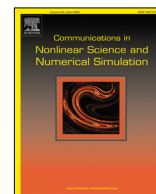




Contents lists available at ScienceDirect

Communications in Nonlinear Science and Numerical Simulation

journal homepage: www.elsevier.com/locate/cnsns

Research paper

Unraveling the highly nonlinear dynamics of KCN molecular system using Lagrangian descriptors

F. Revuelta^{a,*}, F.J. Arranz^a, R.M. Benito^a, F. Borondo^{b,c}^a Grupo de Sistemas Complejos, Escuela Técnica Superior de Ingeniería Agronómica, Alimentaria y de Biosistemas, Universidad Politécnica de Madrid, Avda. Puerta de Hierro 2-4, 28040 Madrid, Spain^b Departamento de Química, Universidad Autónoma de Madrid, Cantoblanco, 28049 Madrid, Spain^c Instituto de Ciencias Matemáticas (ICMAT), Cantoblanco, 28049 Madrid, Spain

ARTICLE INFO

Article history:

Received 27 July 2022

Received in revised form 21 March 2023

Accepted 11 April 2023

Available online 24 April 2023

Keywords:

Molecular vibrations

Invariant manifolds

Lagrangian descriptors

ABSTRACT

In this work, we identify the phase-space structures which are responsible for the chaotic dynamics observed in KCN molecular system using the Lagrangian descriptors. We show that the vibrational dynamics of this molecule is strongly determined by the invariant manifolds associated with a particular stretching periodic orbit previously described (Párraga et al., 2018). Likewise, the representation of these invariant manifolds on a Poincaré surface of section is also studied, concluding that the intricate depiction that is observed has its origin in the complex behavior of the manifolds, which is a consequence of the strong anharmonicities in the potential energy surface.

© 2023 The Author(s). Published by Elsevier B.V. This is an open access article under the CC BY-NC-ND license (<http://creativecommons.org/licenses/by-nc-nd/4.0/>).

1. Introduction

Molecules have an intrinsic rich dynamics that can combine rotational with vibrational motion for a given state. The combination of these motions makes the internal dynamics extremely involved. Then, a detailed description of the problem can be solely conducted when the complexity of their dynamics is reduced using certain approximations, such as the Born–Oppenheimer or adiabatic one. The Born–Oppenheimer approximation separates the electronic motion from the nuclear one due to the large difference that exists among their masses. Furthermore, when rotational motion is neglected and for sufficiently low energies, the motion of atomic nuclei reduce to vibrations around the equilibrium points of the Potential Energy Surface (PES). Then, the frequency of the molecular ground state can be simply estimated using a harmonic approximation to the potential minima, around which stable configurations are formed. In this situation, normal mode analysis can provide valuable information on the molecular properties. Nevertheless, due to their small sizes (of the order of the Bohr radius), the direct observation of the vibrational normal modes has been only very recently achieved [1]. For more excited overtones, i.e., at higher energies, the normal mode analysis starts to break down due to the anharmonicities in the potential. Thus, chaotic motion can take place and nonlinear tools borrowed from dynamical systems theory become more suitable.

Vibrational motion can also play a central role in chemical reactivity: it can enable reactions that would require much larger translational energies for the ground state vibrational mode [2,3]. In that case, the internal vibrational energy of the molecule is transferred to the other degrees of freedom (dofs), and, as a result, the energetic barrier can be eventually overcome and the reaction can happen through the reaction path, defined by the Minimum Energy Path (MEP) of the PES

* Corresponding author.

E-mail addresses: fabio.revuelta@upm.es (F. Revuelta), fj.arranz@upm.es (F.J. Arranz), rosamaria.benito@upm.es (R.M. Benito), f.borondo@uam.es (F. Borondo).

that connects two stable configurations. The consequent rearrangement of the chemical bonds yields the final products. The importance of the excitation of the right bonds as well as the orientation of the molecule has made possible the development of a selective Chemistry.

Simplified pictures of chemical reactions typically focus on the description of the dynamics in the neighborhood of the MEP as it is the prominent route for a reaction to take place [4], i.e., it is the natural way for the molecule to change its configuration by going from one stable configuration (usually known as *reactant*) to the other (the so called *product*) [5]. In the case of systems with 2 dofs, the existence of regular or irregular motion is well established by the Poincaré surface of section (PSOS) along it [6]. Though this tool provides a clear picture of the regular motion as it identifies invariant tori [7], it is not capable, in general, to provide a deep insight into chaotic motion. For this purpose, other chaos indicators are more suitable [8–13].

In this work, we identify the phase space (coordinates and momenta) structures which are responsible for the chaotic dynamics observed in the KCN molecule using the Lagrangian descriptors (LDs). This tool, originally developed to study oceanic transport [14,15], has opened novel routes to the characterization of the chaotic motion observed in chemical systems [16–19]. We demonstrate that the vibrational dynamics of this molecular system is strongly influenced by the invariant manifolds associated with a stretching periodic orbit (PO) sited at the top of the energetic barrier. In many chemical systems such barriers separate them into two different regions (reactants and products), which are connected via the MEP. More importantly, they act as bottlenecks for chemical reactivity. This is the reason why transition state theory computes reaction rates studying this region of phase space, as it is the time-limiting step for a reaction to take place. The geometrical version of transition state theory [20–24] has shown that the manifolds associated with the PO found at the barrier top unambiguously determine whether an initial condition (IC) will yield a reaction or not, this overcoming the old recrossing problem that is responsible for overestimated reaction rates.

The vibrational dynamics of KCN molecular system presents a high degree of chaoticity, even at low energy values. On the one hand, the CN group has a strong triple bond which is responsible for high frequency vibrations of its constituents. On the other hand, the bond between the potassium atom and the CN group is much weaker, this opening the route for large amplitude anharmonic motions of potassium atom far away from the equilibrium point, and then chaos. Furthermore, the different scales in these two motions allows one to set the C–N distance frozen, so the system can be described using a model with only two dofs (see Section 2). Still, the considered energy lies close but below that of the bifurcation where an unexpected stability region, i.e., invariant tori, embedded within the manifolds of two unstable POs emerges. This interesting phenomenon has been previously studied by some of us in Ref. [25]. Let us remark that, below the bifurcation energy, the manifolds related to the previous PO are the only ones which show up automatically on the LD-plots, something that does not happen for the other existing POs. Moreover, we show that the LDs are able to unravel the invariant manifolds only when they are computed for an adequate integration time [14,26], which is related to the stability exponent of the PO of interest. The accuracy of our calculations has been assessed by comparison with the explicit computation of the manifolds by diagonalizing the monodromy matrix. Furthermore, we also discuss some interesting aspects of the PSOS defined along the MEP. By studying the shape of the manifolds on that surface, which is certainly complex, we conclude that the dynamics is much more intriguing than in other triatomic molecules [27].

The outline of this article is as follows. First, we introduce the molecule under study in Section 2. Second, we present the methods used in this work in Section 3. Third, Section 4 is devoted to the results of our study and the corresponding discussion. Finally, we sum up this work by reporting the main conclusions and final remarks of this study in Section 5.

2. System

This section is devoted to the description of the molecule under study: Potassium cyanide, KCN. The vibrational motion of this molecular system can be adequately described using the Jacobi coordinates schematically sketched in Fig. 1(a). Here, the radius R is the modulus of the vector that goes from the center of mass of the cyanide group to the potassium atom, and the coordinate θ is associated with the angle formed by the previous vector and the axial axis along the CN fragment. As the cyanide group has a very rigid triple bond, the higher-frequency vibrations of the CN fragment are neglected, and the CN bond is considered to be frozen at its equilibrium value. Then, vibrational dynamics of the molecule in its rotational ground state is adequately described by the following 2-dofs Hamiltonian

$$\mathcal{H} = \frac{P_R^2}{2\mu_1} + \frac{P_\theta^2}{2} \left(\frac{1}{\mu_1 R^2} + \frac{1}{\mu_2 r_{eq}^2} \right) + V(R, \theta), \quad (1)$$

where P_R and P_θ are the conjugate momenta associated with the R and θ coordinates, respectively, $\mu_1 = m_K(m_C m_N)/(m_K + m_C + m_N)$, and $\mu_2 = (m_C m_N)/(m_C + m_N)$ are reduced masses corresponding to the K–CN and C–N groups, respectively, $r_{eq} = 2.22$ a.u. is the equilibrium distance of the CN group, and $V(R, \theta)$ is the PES produced by the electrons within a Born–Oppenheimer approximation. This PES has been obtained using the adiabatic fitting to the *ab-initio* calculations reported in the Ref. [28]. Likewise, it is very well suited to study the classical dynamics since the derivatives of the potential are in this case very easily computed, contrarily to what typically happens in some realistic molecular potentials. The fundamental domain of this PES is shown as a contour plot in Fig. 1(b). Here, the MEP, which is the natural reaction path, has been also shown superimposed as a dashed cyan line. Four relevant points have been highlighted there. On the one hand, the two circles mark the position of the potential minima, which correspond to two *centers* in the phase space; as a consequence,

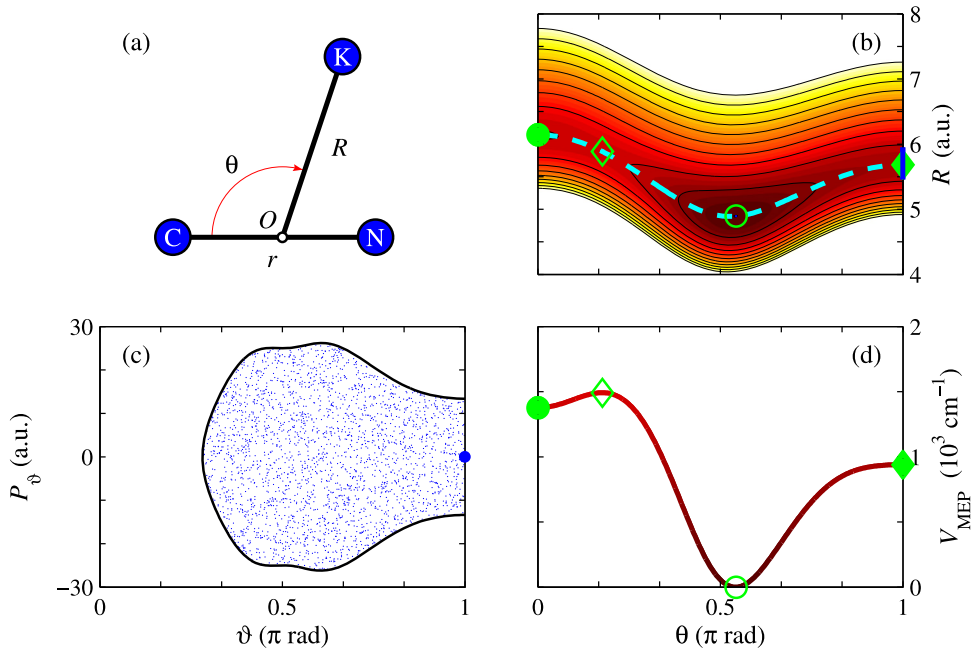


Fig. 1. (a) Definition of the Jacobi coordinates (R, r, θ) for the KCN molecular system, where r -coordinate is kept fixed to its equilibrium value. The point O corresponds to the center of mass of the CN group. (b) Equipotential lines of the potential energy surface for KCN molecule in the fundamental domain. The dashed thick cyan line shows the minimum energy path, which is the natural reaction path. The green circles and diamonds highlight the positions of the stable and unstable equilibrium points of the potential corresponding, respectively, to potential minima (centers) and saddle points. The blue vertical line (at $\theta = \pi$ rad) shows the stretch periodic orbit of interest. (c) The Poincaré surface of section given by Eq. (2) for $E = 1300 \text{ cm}^{-1}$ is formed by a sea of disconnected points, indicating a high chaoticity, within which the position of the periodic orbit of panel (b) has been marked as a blue circle. (d) Potential energy profile along the minimum energy path. The critical points of panel (b) have been marked.

these points are related to the stable conformers of the molecule, and the motion in their neighborhood is well described within the harmonic approximation. Notice also that while the absolute minimum localized at $\theta = 0.542\pi$ rad (empty green circle) is extremely deep (the molecule would require an energy of 1492 cm^{-1} to overcome the energetic barrier found at $\theta = 0.176\pi$ rad), the colinear configuration associated with $\theta = 0$ rad (filled green circle) is confined by a modest barrier of 116 cm^{-1} . On the other hand, the saddle-points sited at the local and absolute maxima of the MEP have been superimposed as filled and empty green diamonds, respectively. Notice the dramatic difference between the CN-K colinear configuration of this molecule and other similar ones (CN-X), being $X = \text{H}$ [29] or Li [18], as in the present case it corresponds to an unstable configuration since it is localized at a saddle point, which opens the route to hyperbolic motion, while in the other cases it corresponds to stable configurations. The stability of the previous points can be better inferred by inspection of Fig. 1(d), where the energy profile along the MEP, defined by $R = R_{\text{MEP}}(\theta)$, is shown.

The molecular system under study, KCN, is very floppy, and then chaotic motion can take place even at very low vibrational energies. To demonstrate this fact, we present in Fig. 1(c) a composite PSOS for $E = 1300 \text{ cm}^{-1}$, a value close to that of the previously mentioned bifurcation [25] and to the energy of the 25th vibrational state (1305 cm^{-1}), (for further examples at different energies, see Ref. [25]). To guarantee that it is an area preserving map, as prescribed by Liouville Theorem [6], we have performed the following canonical transformation

$$\rho = R - R_{\text{MEP}}(\theta), \quad (2a)$$

$$\vartheta = \theta, \quad (2b)$$

$$P_\rho = P_R, \quad (2c)$$

$$P_\vartheta = P_\theta + P_R \frac{dR_{\text{MEP}}(\theta)}{d\theta}. \quad (2d)$$

The PSOS is obtained by representation of the pairs (ϑ, P_ϑ) along the MEP, for $\rho = 0$, and $P_\rho < 0$. Notice that, as the PSOS is defined along the MEP, it is the most likely surface to be crossed by all the trajectories of the system.

From the visual inspection of the PSOS shown in Fig. 1(c) one can certainly claim that the molecular dynamics is very chaotic at the considered energy. Unfortunately, the PSOS can only distinguish between chaotic and regular motion, but its utility for a deeper analysis of the chaotic regions of the phase space is very limited. Then, other methodologies must be applied, like the LDs described in the next section, which have enabled us to identify the invariant structures that are hidden in the PSOS despite of determining the vibrational dynamics of the system, as reported in more detail in Section 4.

3. Methods

In this section we describe the methods that have been used. First, Section 3.1 summarizes the definition and the most important properties of the LDs, the tool that we have successfully applied to identify the invariant manifolds associated with a particular PO that seems to determine the global vibrational dynamics of KCN molecular system. Second, Section 3.2 revisits the traditional computation of the previous invariant manifolds which is based (i) on the linear study of their stability via the monodromy matrix, and (ii) on the numerical propagation of initial conditions lying in the tangent space.

3.1. Lagrangian descriptors

In order to study the chaotic structure of the phase space of KCN we use the LDs, which for a system with N equations of motion ($N/2$ dofs) are defined as [26,30]

$$M_{\pm}(\mathbf{z}_0, \tau) = \pm \sum_{i=1}^N \int_0^{\pm\tau} |\dot{z}_i(t)|^p dt, \quad (3)$$

where

$$\dot{z}_i = \mathbf{J} \frac{\partial \mathcal{H}}{\partial z_i}, \quad \text{with } \mathbf{J} = \begin{pmatrix} \mathbf{0}_{N/2 \times N/2} & \mathbf{I}_{N/2 \times N/2} \\ -\mathbf{I}_{N/2 \times N/2} & \mathbf{0}_{N/2 \times N/2} \end{pmatrix}, \quad (4)$$

are the equations of motion (EoM), in our case associated with the Hamiltonian (1), with $0 < p < 1$, and the vector of ICs. $\mathbf{z}_0 = (R_0, \theta_0, P_{R,0}, P_{\theta,0})$ for the system under study (where $N = 2$). As already observed for other molecular system [18,19], a value $p = 0.4$ is adequate. Let us remark that similar results would be obtained for other values of p close to 0.4, e.g. 0.5. Notice that Eq. (3) allows the independent identification of the stable and unstable manifolds all at once by simply adding the LDs computed forward, M_+ , and backwards, M_- , in time, as in the original definition introduced by Lopesino et al. in the Ref. [31]. One can also determine the LDs using other metrics as long as they are positive. Our choice is computationally more efficient than the original definition based on the arc length [14] since it is able to unveil the invariant manifolds using shorter integration times.

3.2. Linear-stability analysis of periodic orbits

In this section we revisit the fundamentals on the linearized classical motion, which have been used in the computation of the invariant manifolds to test the validity of the LDs. Further details can be found in Refs. [32,33].

Let us consider a PO in phase space $\mathbf{z}_{PO}(t)$ that solves the EoM (4) for the IC $\mathbf{z}_{PO,0} = \mathbf{z}_{PO}(0)$. This trajectory is periodic in time, so that $\mathbf{z}_{PO}(T) = \mathbf{z}_{PO,0}$, with T the period. If we consider now a different IC $\mathbf{z}_0 = \mathbf{z}_{PO,0} + \delta\mathbf{z}_0$, the two trajectories will be separated a distance equal to $\delta\mathbf{z}(t) = \mathbf{z}(t) - \mathbf{z}_{PO}(t)$ after a certain time, t . For sufficiently small displacements, there is a linear relationship between $\delta\mathbf{z}(t)$ and $\delta\mathbf{z}_0$,

$$\delta\mathbf{z}(t) = \mathcal{M}(t)\delta\mathbf{z}_0, \quad (5)$$

where the matrix $\mathcal{M}(t)$ satisfies that

$$\dot{\mathcal{M}}(t) = \mathcal{L}\mathcal{M}(t), \quad \mathcal{M}(0) = \mathbf{I}, \quad (6)$$

with $\mathcal{L} = \mathbf{J} \frac{\partial^2 \mathcal{H}}{\partial z^2} \Big|_{\mathbf{z}_{PO}}$ the linearized flow along the trajectory. The matrix $\mathcal{M}(t)$ is symplectic ($\mathcal{M}^+(t)\mathbf{J}\mathcal{M}(t) = \mathbf{J}$), and, after one period of time, $\mathcal{M} \equiv \mathcal{M}(T)$ is called *monodromy matrix*.

For systems with 2 dofs, the matrix \mathcal{M} has dimension 4, and then it also has 4 eigenvalues. Two of them are equal to 1, so their corresponding eigenvectors describe trivial directions of motion, where $\delta\mathbf{z}(T) = \delta\mathbf{z}_0$. One of these eigenvectors is parallel to the PO. Thus, the initial displacement cannot change due to the periodic behavior of the trajectory. The other trivial eigenvector corresponds to a displacement leaving the energy shell, whose projection perpendicular to the energy is also conserved as the energy remains constant in the case of conservative systems like the one under study (cf. Eq. (1)). Accordingly, the nontrivial contributions of the \mathcal{M} matrix describe the evolution of displacements perpendicular to the PO on the energy shell, which can be totally described using a 2×2 transversal matrix. This transversal matrix has two eigenvalues, which can be real or complex, being their product 1.

For stable POs, the eigenvalues of the transversal monodromy matrix form a complex-conjugate pair. For unstable POs they are real and satisfy that $|\Lambda_u| = |\Lambda_s|^{-1}$; in this case, they are also usually recast as a function of the Floquet exponents $\lambda_{u,s}$ as $\Lambda_{u,s} = \pm \exp(\lambda_{u,s}T)$, where the sign $+$ ($-$) corresponds to a hyperbolic (hyperbolic with reflection) PO. The corresponding eigenvectors $\zeta_{u,s}$ are parallel to the invariant manifolds at the considered point. The time-evolution of an IC lying on them is prescribed by Eq. (5), but it can be more easily understood with the help of Floquet analysis. This theory allows the decomposition of the matrix \mathcal{M} as the product of a periodic matrix associated with a rotation around the PO, and a hyperbolic matrix that accounts for the dilation-contraction motion. Due to the combination of the previous motions, an IC located on the unstable eigenvector ζ_u will separate from the PO in the corresponding (rotated) direction.

Conversely, an IC located on the stable eigenvector ζ_s will approximate to the PO in the corresponding (rotated) direction. After one period of time, the IC will map on the same direction, but separated a distance equal to $|\delta_{u,s}(T)| = |\delta_0| \exp(\lambda_{u,s}T)$. Opposite behavior is observed when the ICs are evolved backward in time, i.e., ICs lying on the unstable manifold will approximate to the reference PO, while those on the stable manifold will separate from it. A general IC describes a rotation around the reference PO while performing a combined dilation-contraction motion along the unstable-stable eigenvector ζ_s - ζ_u , i.e., the unstable-stable manifolds.

To summarize, the stable and unstable manifolds can be computed by diagonalizing the transversal monodromy matrix, and following the time-evolution of ICs localized on the corresponding eigenvectors. Since the manifolds are *invariant* structures, these ICs always map on them. Thus, if one takes a sufficiently high number of ICs, the corresponding trajectories will represent the manifolds in the phase space. The unstable manifold can be reconstructed by propagating ICs lying in its linear region forward in time, while the stable one is computed by propagating the ICs backwards.

4. Results and discussion

In this section, we present the results of our study of the KCN molecular system for a vibrational energy of 1300 cm^{-1} , a value just below that where the bifurcation responsible for the emergence of an unexpected stability region appears [25]. This section is divided in two parts. First, we introduce in Section 4.1 the invariant manifolds that are responsible for the chaotic motion. Second, we discuss in Section 4.2 the complex structure of the previous objects when represented on the PSOS defined along the reaction path of the molecule.

4.1. Identification of the invariant manifolds using the Lagrangian descriptors

Figs. 2(a) and 2(c) show the LDs as defined in Eq. (3) for the KCN molecule under study. Fig. 2(a) shows the forward LD, M_+ , while Fig. 2(c) corresponds to the backward LD, M_- , computed for a uniform mesh of ICs on the energetically accessible region of the composite PSOS shown in Fig. 1(c). A clear structure is visible in both figures that is associated with the invariant manifolds of a stretching PO defined by $(\theta, P_\theta) = (\pi, 0)(\text{rad}, \text{a.u.})$, which exists at the top of the lowest energetic barrier ($\theta = \pi \text{ rad}$).

To demonstrate the previous assessment, we show in Figs. 2(b) and 2(d) an explicit calculation of the invariant manifolds of interest following the procedure reported in Section 3.2. For this purpose, the corresponding monodromy matrix has been first diagonalized. Then, a set of 10^4 ICs on its eigenvectors has been time-propagated by numerically integrating Eq. (4) for the Hamiltonian (1). In order to assess the validity of the linear approximation to the manifolds all the ICs lie sufficiently close to the fixed point. In particular, the ICs for the stable manifold are given by $(9.94725\pi \text{ rad}, 0.50343 \text{ a.u.}) \times 10^{-5}k$, with $k = 1, 2, \dots, 10^4$, while those for the unstable manifold satisfy that $(9.94750\pi \text{ rad}, -0.50369 \text{ a.u.}) \times 10^{-5}k$. For the stable manifold the composite PSOS shown in Figs. 2(b) has been computed using evolving backward in time of the ICs over 1700 fs, while that for the unstable manifold presented in Figs. 2(c), has been computed by the ICs over the same time but forward. In general, for the evolution time under consideration, the trajectories lead by the previous ICs have 14 intersections with the PSOS, though some of them have 15 or even 16 crossings (in both cases, the mostly-crossing ICs represent less than 10% of the total number of ICs considered). The subsequent iterations on the PSOS separate more and more from the PO due to its hyperbolic character.

As can be inferred by comparison of Figs. 2(a) and 2(b), on the one hand, and Figs. 2(c) and 2(d), on the other hand, the LD-plots clearly unveil the invariant manifolds that were conversely not visible on the PSOS shown in Fig. 1(c). Note that while the LD-plots shown in Figs. 2(a) and 2(c) have been computed by integrating Eq. (3) forward and backward in time, respectively, the manifolds presented in Figs. 2(b) and 2(d) have been calculated by integrating the Hamilton EoM (4) for reverse time. The reason for this is the following: due to the *invariant* character of the manifolds, any IC evolves remaining on them for all times. In particular, an IC on the stable manifold approximates the PO, while an IC starting on the unstable manifold moves apart from it with an evolution forward in time. Similarly, an IC on the stable manifold separates from the PO, while an IC starting on the unstable manifold approximates to it with an evolution backward in time. On the contrary, those ICs that lie outside the manifolds tend to asymptotically approximate to one of them. More specifically, the trajectories with ICs outside the stable manifold approximate the unstable one when evolved forwards in time, and the trajectories with ICs outside the unstable manifold approximate the stable one when evolved backwards in time. This distinct dynamical behavior introduces a singularity in the value of the LDs for ICs lying on the manifolds, which enables their identification in the LD plots [31].

Let us conclude the discussion of Fig. 2 by solving the EoM (4) for a set of ICs that lie on the manifolds for reverse time, namely, forward in time for the unstable manifold, and backwards in time for the stable manifold. The reason is that if this calculation is performed in the same way as for the LDs, all ICs would (*quickly*) end up on the PO, i.e., on the PSOS fixed point corresponding to $(\vartheta, P_\vartheta) = (\pi \text{ rad}, 0 \text{ a.u.})$, due to their hyperbolic nature (see Section 3.2), and then no large, more global, structure would become visible.

According to dynamical systems theory, the invariant manifolds determine the phase-space dynamics in the neighborhood of the corresponding PO. Thus, the dynamics of potassium atom when overcoming the energetic barrier located at $\theta = \pi \text{ rad}$ will be determined by them, a fact that has enabled novel perspectives into transition state theory [21,23,29,34,35]. But the importance of the observed phase space structures goes beyond that region: They certainly

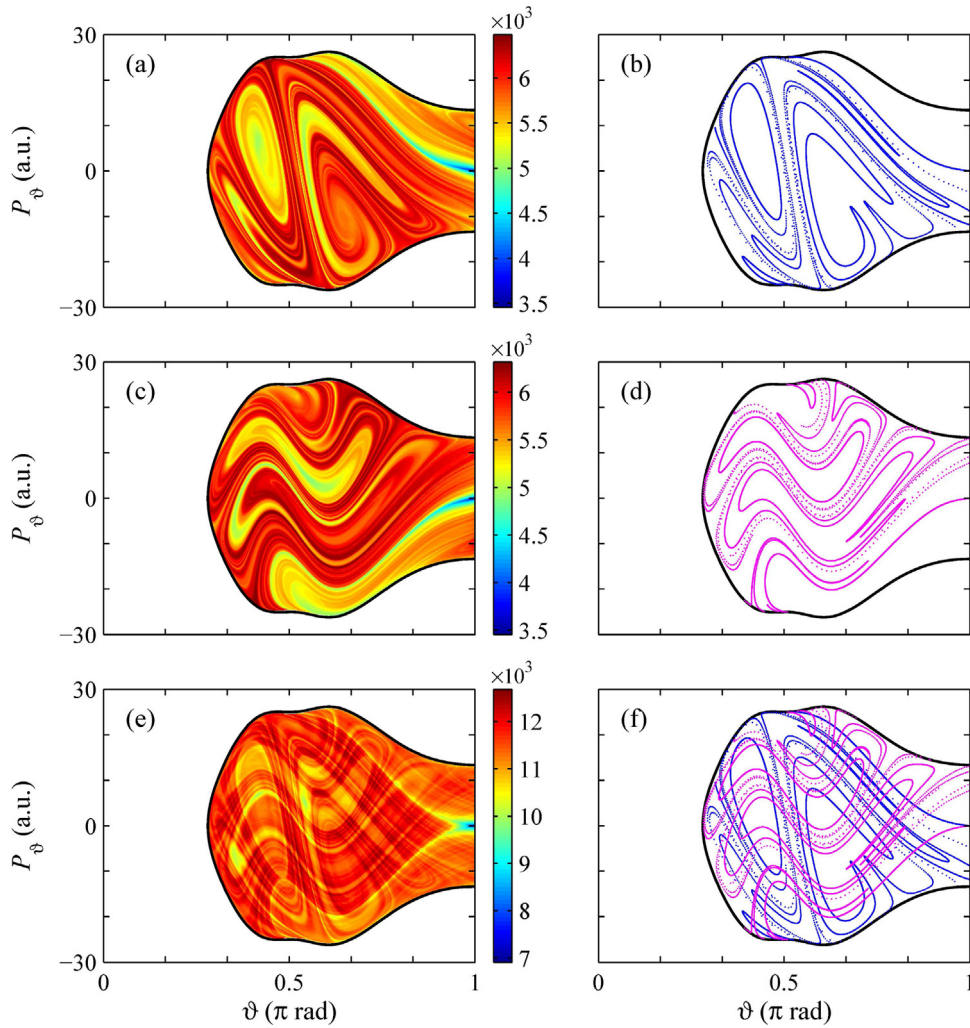


Fig. 2. Cuts of the phase space of the KCN molecular system along the Poincaré surface of section given by Eq. (2) for a vibrational energy $E = 1300 \text{ cm}^{-1}$. Lagrangian descriptors integrated (a) forward, M_+ , and (c) backwards, M_- , as defined in Eq. (3) for $\tau = \tau_{\text{ref}} = 437.5 \text{ fs}$, and (e) the homoclinic tangle shown by their summation. (b) Stable and (d) unstable invariant manifolds associated with the hyperbolic fixed point $(\vartheta, P_\vartheta) = (\pi, 0) (\text{rad, a.u.})$, whose (f) superposition shows the homoclinic tangle in the KCN molecular system. The number of initial conditions equals 10^4 distributed in a uniform mesh [panels (a), (c), and (e)], or along the linear region of the manifolds [panels (b), (d), and (f)].

have an influence on the global dynamics of the system, as demonstrated by the fact that they naturally emerge in the LD-plots shown in Figs. 2(a) and 2(c) despite the fact that the ICs were taken uniformly distributed over the PSOS, and no additional information on that particular stretching PO was included.

One crucial step in the LDs computation is the selection of an adequate integration time [14]. If this time is too short, then the LD-plots show up as blurred pictures, where no recognizable pattern can be identified. Contrary, very large integration times lead to a too detailed description of the invariant manifolds, which enhances their local differences and their identification becomes more difficult. Then, the trajectories become much larger, and, as a consequence, the exponential dependence on the initial conditions yields wild oscillations in the LDs and then a pointillist-like picture on the plot [26]. Consequently, the selection of an adequate computation time able to distinguish the hyperbolic signatures in phase space becomes critical. Such a suitable time depends solely on the stability exponent of the invariant manifolds of interest. In this paper, the LDs shown in Figs. 2(a) and 2(c) have been calculated using a time equal to $\tau_{\text{ref}} = \lambda^{-1} = 437.5 \text{ fs}$, being λ the Floquet exponent associated with the unstable manifold of the stretching PO shown in Figs. 1(b) and 1(d). This time is approximately only four times larger than the period of the corresponding PO ($T = 110.8 \text{ fs}$).

Before concluding this section, let us discuss what happens for other integration times. Figs. 3 and 4 show the value of the LDs along the PSOS (2) for three integration times smaller and larger than τ_{ref} , respectively. The results on the left (right) columns show the value of M_+ (M_-), which have been obtained by forward (backward) integration of Eq. (3). Figs. 3(a) and 3(b) show the LDs for $\tau = \tau_{\text{ref}}/10$. As can be seen, the LD-plots are slow varying functions, which is an

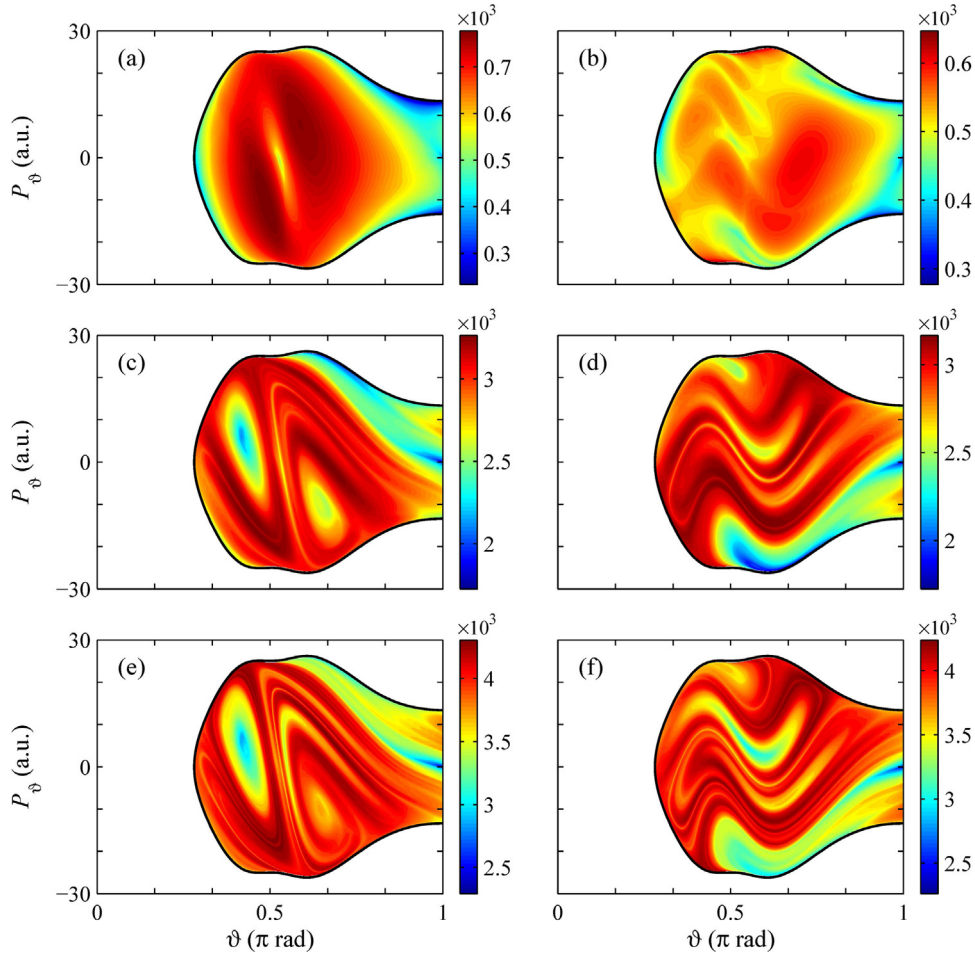


Fig. 3. Lagrangian descriptors integrated (left) forward, M_+ , and (right) backwards, M_- , as defined in Eq. (3) along the Poincaré surface of section given by Eq. (2) for a vibrational energy $E = 1300 \text{ cm}^{-1}$, and $\tau = \tau_{\text{ref}}/10$ (top), $\tau = \tau_{\text{ref}}/2$ (middle), and $\tau = \tau_{\text{ref}}/1.5$ (bottom), being $\tau_{\text{ref}} = 437.5 \text{ fs}$. The number of initial conditions equals 10^4 distributed in a uniform mesh.

indication that the integration time is too small to capture the distinct character of the invariant manifolds. The imprint of the invariant manifolds on the LD-plots starts to become visible only for longer times. Their presence can be inferred from Figs. 3(c) and 3(d), which are associated with $\tau = \tau_{\text{ref}}/2$, and can be more clearly observed in Figs. 3(e) and 3(f), which correspond to a longer integration time $\tau = \tau_{\text{ref}}/1.5$. When the integration time is not much larger than τ_{ref} , as shown in Figs. 4(a) and 4(b), which correspond to $\tau = 1.5\tau_{\text{ref}}$, plots similar to those shown in Fig. 2(e) and 2(f) are obtained. As in those cases, the stable and unstable manifolds can be clearly identified. The manifolds are similarly visible for an integration time of $\tau = 2\tau_{\text{ref}}$, as shown in Figs. 4(c) and 4(d). The integration over much longer integration times is, nevertheless, less useful. Then, the local properties of the manifolds are included, and hence they are no longer visible as continuous lines. In this way, when an integration time of $\tau = 10\tau_{\text{ref}}$ is used, the invariant manifolds are much harder recognizable, as inferred by visual inspection of Figs. 4(e) and 4(f). In summary, the results reported indicate the necessity of an adequate integration time is compulsory for the correct identification of the invariant manifolds. The accuracy of the LDs has been also previously assessed in the literature by performing similar comparisons in other systems (see, e.g., Refs. [17,26,36,37], and references therein).

The chaotic motion inferred from the visual inspection of the composite PSOS presented in Fig. 1(c) is a consequence of the complex structure of Fig. 2 just discussed. Actually, the homoclinic intersections between the stable and unstable manifolds of the system yield an extremely intriguing dynamics. Such intersections can be observed in Fig. 2(e), where Figs. 2(a) and 2(c) have been added, as well as in Fig. 2(f), where Figs. 2(b) and 2(d), have been superimposed. As can be seen, the invariant manifolds intersect the PSOS dozens of times, forming the famous homoclinic tangle that originates the chaotic motion. Notice, however, that this tangle is not formed by a single continuous line, despite of being the manifolds continuous structures. Conversely, it is constituted by a set of open lines that disappear at the PSOS boundary, and other curves that are closed. We present in the incoming section a thorough analysis of this complex shape.

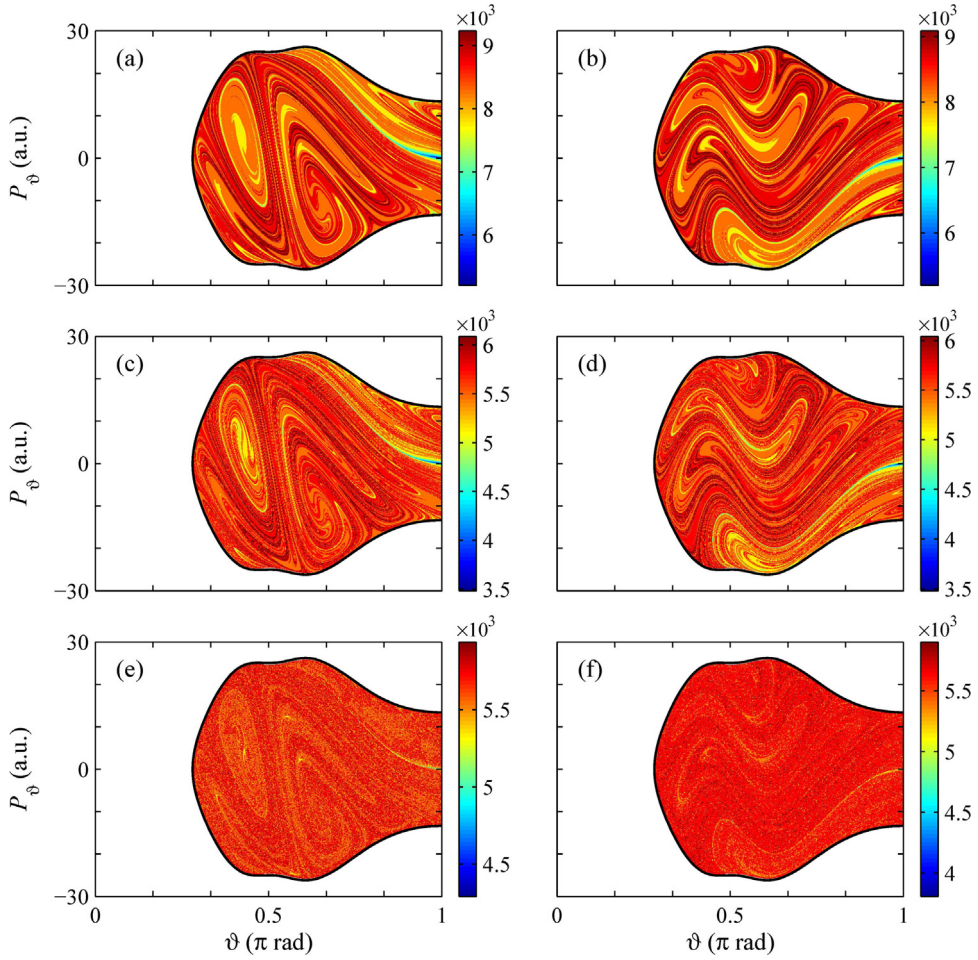


Fig. 4. Same as Fig. 3 for three integration times larger than τ_{ref} , namely: $\tau = 1.5 \tau_{\text{ref}}$ (top), $\tau = 2 \tau_{\text{ref}}$ (middle), and $\tau = 10 \tau_{\text{ref}}$ (bottom).

4.2. Representation of the invariant manifolds on the Poincaré surface of section

In this section, we provide a better understanding of the representation of the invariant manifolds on the composite PSOSs shown in the right column of Fig. 2. For this purpose, we first discuss the critical points of the representation of the manifolds on the PSOSs computed for shorter times in Section 4.2.1. Second, we present in Section 4.2.2 a three-dimensional representation of the time-evolution of the manifolds which renders more simple pictures as there are less crossing points.

4.2.1. Reconstruction of the invariant manifolds

Figs. 5 and 6 show, respectively, the composite PSOSs of the invariant manifolds computed for shorter times, which renders more simple pictures as there are less crossing points. As in the PSOSs shown in Fig. 2, a set of 10^4 ICs has been considered. In this case, however, a more detailed description of the trajectories yielded by each IC has been performed by plotting in a different color the intersection of each orbit with the PSOS.

Figs. 5(a) and 6(a) show the PSOSs obtained when crossed six times by the trajectories. In this case, as well in any other one where few intersections with the PSOS are considered, i.e., short-time evolutions are conducted, the ICs map on short straight lines as they remain in the linear region of the manifolds. This is a well known result in dynamical systems theory: The manifolds emerge on the PSOS as straight lines from the hyperbolic point due to the harmonic character of the PES around it (see discussion in Section 3.2). The anharmonic behavior of the manifolds becomes visible only for longer times. For example, after 11 iterations the stable manifold is clearly distorted upwards, while the unstable one points downwards, as concluded from inspection of Figs. 5(b) and 6(b).

Nonetheless, the real complexity of the dynamics becomes manifest for even longer times. When 12 intersections with the PSOS are considered, some of those ICs considered that lied closer to the reference PO map on the same line already visible in Figs. 5(a) and 5(b) until they reach the top line of the energy boundary for $\vartheta \approx \pi/2$ rad. In principle, one

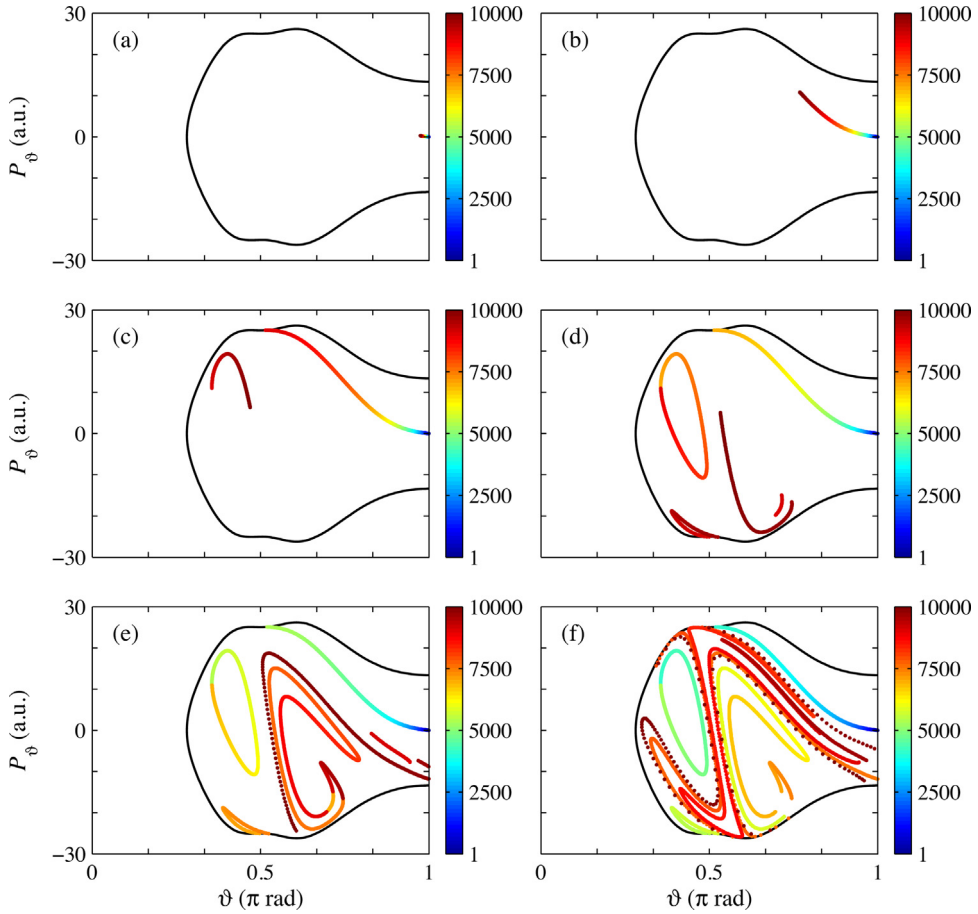


Fig. 5. Poincaré surface of section of the trajectories emerging from a set of 10^4 initial conditions (each one plotted with the color indicated in the colorbar) lying on the linear region of the stable manifold which is found in the close vicinity of the stretch periodic orbit $(\theta, P_\theta) = (\pi, 0)$ (rad, a.u.). The time evolution has been conducted backwards in time up to a particular time for each trajectory, such that 6 (a), 11 (b), 12 (c), 13 (d), 14 (e), and 15 (f) crossings with the Poincaré surface of section are observed.

would expect that the stable manifold that “disappears” at the upper part for $\vartheta \approx \pi/2$ rad, would reappear at the lower part for the same value of ϑ , and in the same way, the unstable manifold that “disappears” at the lower part, would reappear at the upper part. However, those ICs that lied far away from the PO map on an isolated line localized in the region where $0.3\pi \leq \vartheta \leq 0.5\pi$ rad, and $5 \leq P_\theta \leq 20$ a.u., as shown in Fig. 5(c). Note, contrary, in Fig. 6(c) that for the same number of iterations with the map, the ICs lying on the unstable manifold keep on mapping on it (though its shape becomes more involved). After 13 iterations, as shown in Fig. 5(d), the isolated line introduced closes, and other lines emerge on the PSOS. For longer time evolutions, like those used in Fig. 5(e) (14 iterations) or Fig. 5(f) (15 iterations), the previous lines close, and other lines appear on the boundary, this yielding a very complicated pattern, which is responsible for the chaotic motion. Similar comments apply for the unstable manifold. Nevertheless, for the set of ICs considered, in this case 13 iterations of the Poincaré map are required in order to observe the first discontinuity on the manifold. An analogous behavior is observed when more iterations are considered, as done in Figs. 6(e) (14 iterations) and 6(f) (15 iterations). As discussed in the next section, the observed manifolds’ discontinuities appear only on the PSOS due to the strong nonlinearities but not when represented in their full dimension.

4.2.2. Origin of the discontinuities of the manifolds on the PSOS representation

In this section, we present a detailed study of the manifolds previously shown on the PSOS represented in Figs. 5 and 6 (as well as in Figs. 2(b), 2(d), and 2(f)) in order to shed light on their structure on the PSOS. For this purpose, we show in Fig. 7 the time evolution of solely 60 ICs instead of 10^4 as previously done in Sections 4.1 and 4.2.1. As in the mentioned examples of the previous sections, the ICs have been taken on the linear part of the manifolds gotten after having diagonalized the monodromy matrix. In all the simulations shown in Fig. 7, the final time is such that it allows the observation of the first discontinuity in the invariant manifolds when mapped onto the PSOS (12th crossing for the stable manifold, 13th crossing for the unstable manifold). Recall, nonetheless, that due to the different hyperbolic

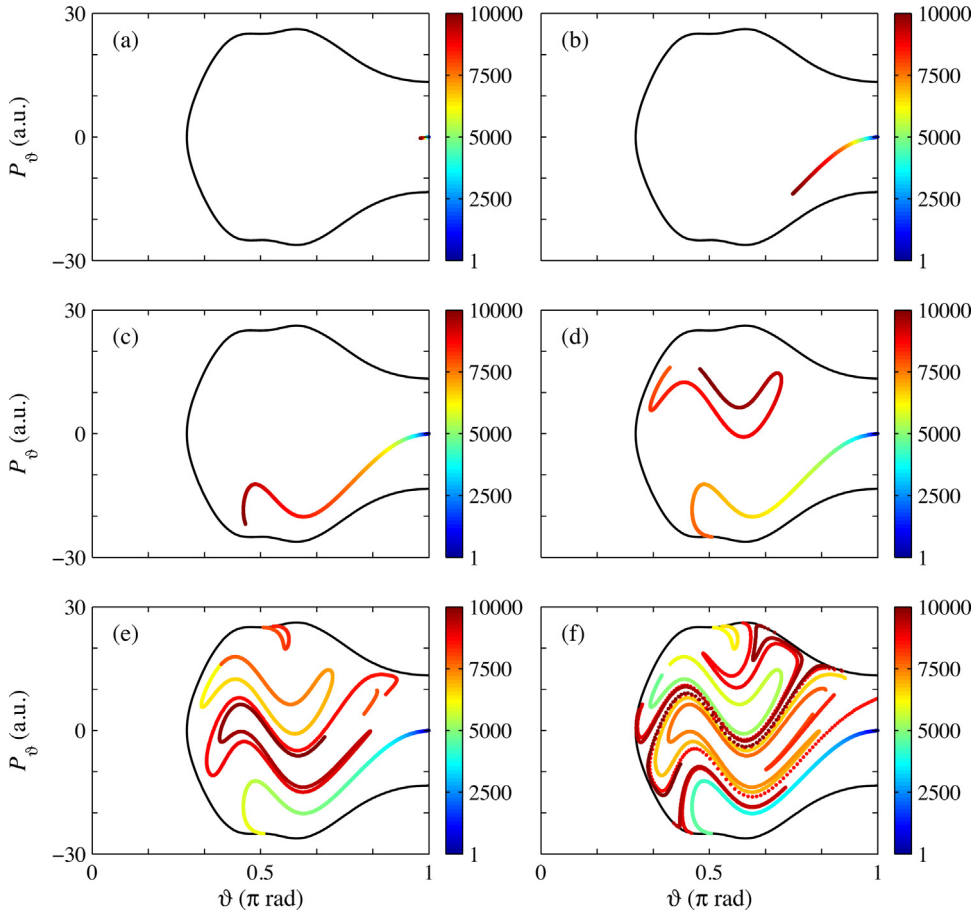


Fig. 6. Same as Fig. 5 for initial conditions lying on the unstable manifold, and evolved forward in time.

character of the manifolds, this time is negative in the case of the stable manifold and positive in the unstable one, being of order ~ 1400 fs in both cases.

Fig. 7(a) unveils the behavior of the stable manifold when the first PSOS discontinuity takes place. Here, some of the final crossing points, which correspond to the 12th intersection with the PSOS, have been labeled with the IC number. All the ICs labeled as 1–54 map onto the continuous gray line emerging from the saddle point. However, due to the highly nonlinear dynamics, a discontinuity takes place at the PSOS edge for $\vartheta \approx \pi/2$ rad, where the manifold “jumps” from the energy boundary to the point $(\vartheta, P_\vartheta) = (0.358\pi, 13.877)$ (rad, a.u.), where it continues mapping along a different line. Consequently, the ICs 55–60 map onto a different (gray) line of the PSOS, rendering the closed loop shown in Fig. 2(c). This unexpected behavior can be better understood by representing the manifold in the three-dimensional $(\rho, \vartheta, P_\vartheta)$ phase space rather than uniquely on the reduced dimensional map given by the PSOS. For this purpose, we show in Fig. 7(c) the projection of the corresponding colored trajectories on the ϑ - P_ϑ plane. Notice that the grayish parts of the orbits correspond to the regions where $\rho < 0$, as concluded by visual inspection of the results in the three-dimensional space presented in Fig. 7(e). These two figures provide an explanation for the unexpected behavior. On the one hand, the trajectories associated with ICs 1–54 oscillate in a quite regular fashion around the $\rho = 0$ plane within the range $-0.2 \text{ a.u.} \leq \rho \leq 0.3 \text{ a.u.}$ for all considered times. In these cases, the momentum P_ρ only changes once its sign between each of the crossings with the $\rho = 0$ plane so they always move first apart from this surface and then start to get closer to it again. On the other hand, the trajectories related to the ICs 55–60 present a similar behavior for small times, and then they map along the same line on the PSOS (see discussion above). However, on their way towards the last mapped point the dynamics becomes more complex. Notice in particular the trajectory associated with the IC number 55. On its way towards the last mapped point (marked as 55 in Fig. 7(a)), this trajectory approaches the $\rho = 0$ plane close to $\vartheta \approx \pi/2$ rad, but then the momentum P_ρ changes its sign, so the trajectory moves away from the PSOS. Subsequently, the sign of momentum P_ρ changes again, and the trajectory approaches once more the PSOS until it eventually crosses it. This fact is a consequence of the highly nonlinear dynamics that occurs for sufficiently long times, and then affects, especially, the latter trajectories, which show similar kind of “irregular” behavior.

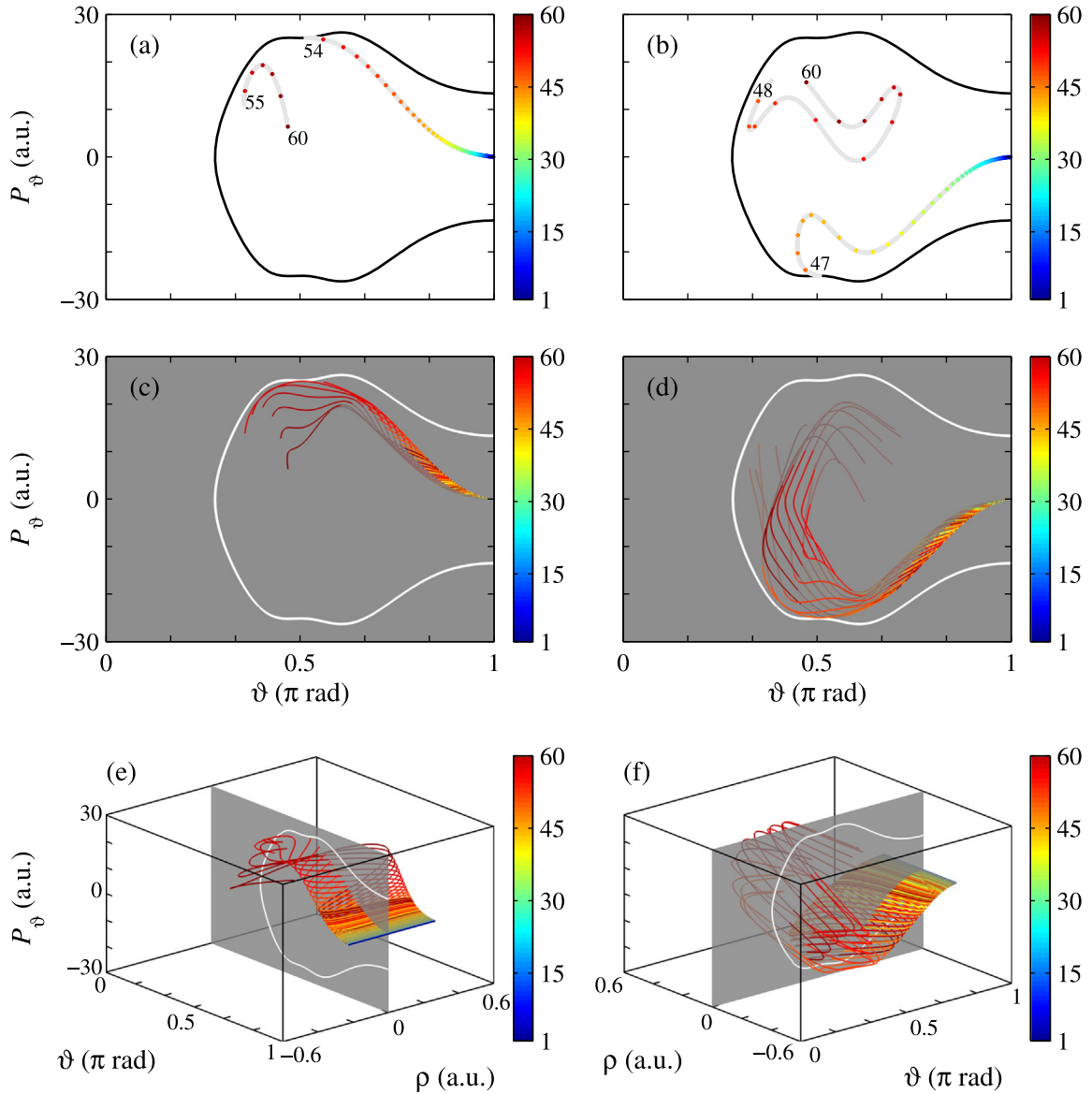


Fig. 7. The time evolution of several neighboring trajectories that lie on the invariant manifolds associated with the stretch periodic orbit $(\vartheta, P_\vartheta) = (\pi, 0)(\text{rad}, \text{a.u.})$ provides a deeper insight on the complex pattern that is observed in the Poincaré surface of section (PSOS) shown in Fig. 2. In this case, 60 initial conditions with $E = 1300 \text{ cm}^{-1}$ and lying on the linear part of the stable (left panels) and unstable (right panels) manifolds of the hyperbolic fixed point $(\vartheta, P_\vartheta) = (\pi, 0)(\text{rad}, \text{a.u.})$ lead to the discontinuous graphical representation on the PSOS. Final time for the stable manifold corresponds to the 12th crossing of the PSOS, and to the 13th crossing for the unstable manifold. Colorbar scale identifies the number of the initial condition. (a)–(b): Composite PSOS for stable and unstable invariant manifolds, where indicative initial condition numbers have been marked at the final crossing point. (c)–(d): Projection of the trajectories, for stable and unstable invariant manifolds, respectively, on the ϑ – P_ϑ plane for $\rho = 0$ (gray). (e)–(f): Three-dimensional representation of the trajectories in $(\rho, \vartheta, P_\vartheta)$ space for stable and unstable invariant manifolds, along with the $\rho = 0$ plane (gray).

Let us conclude the discussion of the stable manifold by describing its mapping on the PSOS for longer times than those discussed above (when the manifold crosses up to 12 times the PSOS). To begin with, the manifold maps clockwise from the point marked as 60 in Fig. 7(a) or until it defines the closed loop shown in Figs. 2(a), 2(b), 5(d), 5(e), and 5(f). Then, a second PSOS discontinuity is observed, and the manifold manifests as a small lobe at the bottom of the PSOS associated with the ICs 55–58, as shown in Fig. 8(a). In our case, this new lobe is defined, among others, by the four red trajectories that map on the same region of the bottom of the PSOS, as inferred from inspection of Fig. 8(c). From there on, the map of the manifold is formed by a series of closed and open curves that fold along each other. The first of these additional lobes corresponds to that marked with the points 59 and 60 in Fig. 8(a), which correspond to the two red trajectories

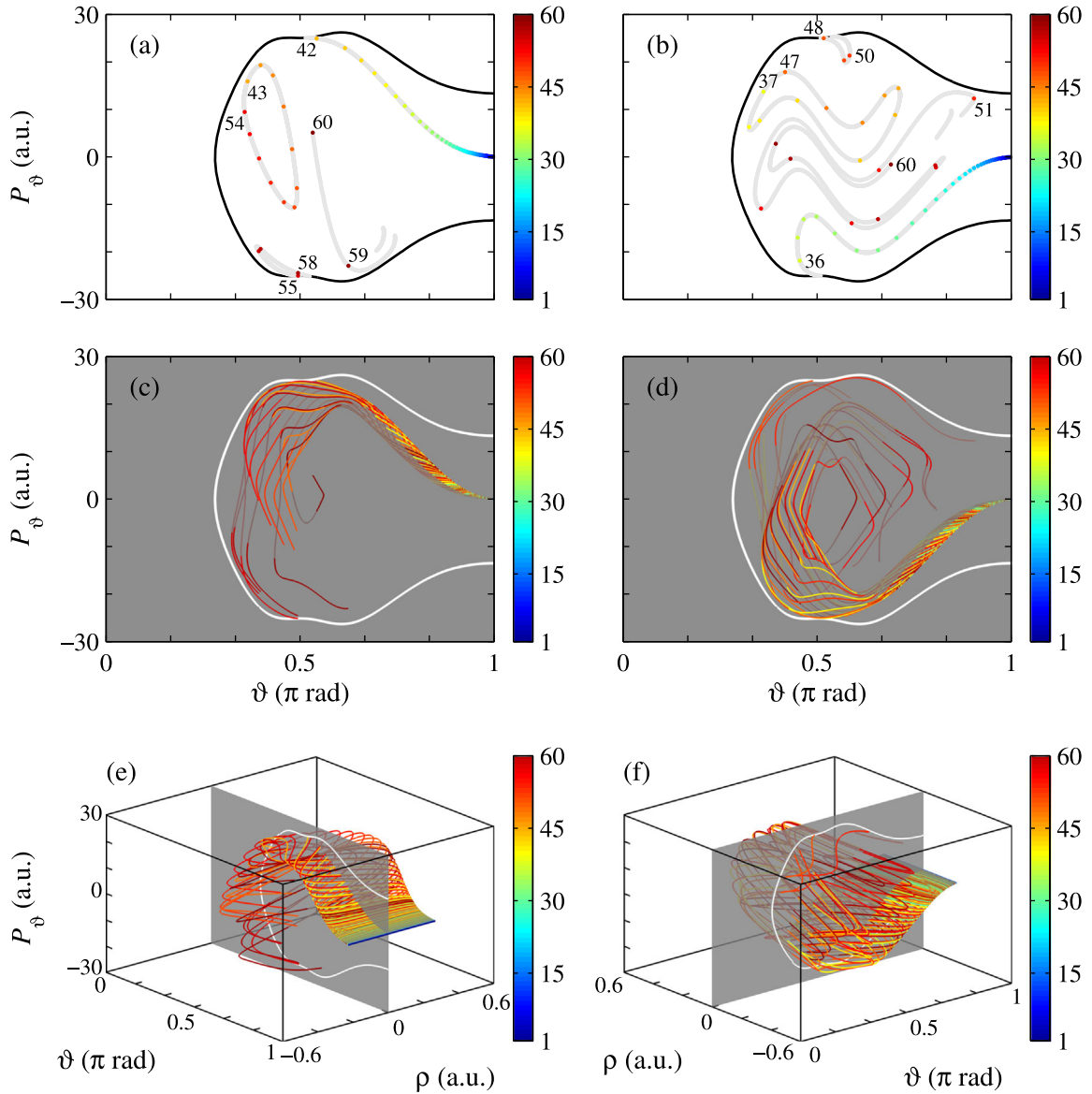


Fig. 8. Same as Fig. 7 for the next crossing of the Poincaré surface of section, namely, the 13th iteration for the stable manifold, and the 14th iteration for the unstable one.

of Fig. 8(c) that are separated from the remaining ones with the same color. Overall, note the intricate dynamics of the trajectories in the three-dimensional representation shown in Fig. 8(e).

The unstable manifold maps on the PSOS in an analogous fashion to that of the stable manifold just discussed. Namely, the PSOS-plot is formed by a collection of open and closed folding curves, as shown in Figs. 2(c), 2(d), 6(e), and 6(f). Nonetheless, for a similar set of ICs on the linear part of the manifolds, the first PSOS discontinuity is not associated with the IC number 54 but 47, as shown in Fig. 7(b). As a consequence, the ICs 48–60 are the only ones which are mapped on the first closed curve that is observed. As in the stable manifold, the discontinuity appears for $\vartheta \approx \pi/2$ rad, but in this case at the bottom part of the PSOS due to the different time evolutions for the points 48–60, as shown in Figs. 7(d) and 7(f). This result can be explained due to the different orientation of the unstable vector of the monodromy matrix. Notice also that in this case the points 48–60 map on the closed curve counterclockwise. This fact can be explained due to the different time evolution in Figs. 7(a) and 7(b); recall that while the PSOSs associated with the stable manifold have been conducted backwards in time, those related with the unstable manifold have been performed forward in time. Figs. 8(b), 8(d), and 8(f) show the unstable manifold for longer integration times. Similar comments as those for the stable manifold apply here.

In summary, the invariant manifolds are surfaces embedded in the phase space, whose intersection with the PSOS results in the one-dimensional discussed curves. In the close vicinity of the saddle point, the manifolds are planes. As a consequence, their intersections with the PSOS yield straight lines, this denoting the harmonic behavior of the PES in that region. As the distance from the PO is increased, the manifolds start to get distorted due to the anharmonicities of the potential which are responsible for the highly nonlinear dynamics of the KCN molecular system. Then, when mapped onto the PSOS they show up as curved lines away from the saddle. In particular, the strong deformation of the manifolds becomes first clearly visible for $\vartheta \approx \pi/2$ rad, where the strong nonlinearities are responsible for a more complex dynamics which is responsible for the emergence of a discontinuity in the PSOS-map. Thus, the manifolds map on a closed curve for a certain number of iterations. For longer time-evolutions, the manifolds further map on a set of folding closed and open curves which are responsible for the highly nonlinear behavior of KCN molecule due to the strong anharmonicities in the potential.

5. Conclusions and final remarks

In this work, we have applied the Lagrangian descriptors to identify the invariant manifolds associated with the stretching periodic orbit of KCN molecule sited at top of the potential energy barrier localized at $\theta = \pi$ rad. These structures show up automatically when solving the equations of motion for initial conditions on a characteristic Poincaré surface of section, and an appropriate integration time is used. Such a proper time is given by the inverse of the stability exponent of the manifolds of the periodic orbit under study (or a value close to it). The stable manifold shows up as a singularity in the plots of the Lagrangian descriptors computed forward in time. Similarly, the unstable manifold shows up as a singularity in the plots of the Lagrangian descriptors computed backward in time. The accuracy of our computations has been assessed by comparison with the manifolds calculated after diagonalizing the monodromy matrix of the periodic orbit of interest and performing a time propagation of initial conditions located on its eigenvectors, i.e., on the linear region of the manifolds. The fact that the computed manifolds show up naturally, while those associated with other existing periodic orbits do not, demonstrates their importance for the vibrational dynamics of the molecule, even far away from the region where the periodic orbit is sited.

Contrary to the Lagrangian descriptors, the Poincaré surface of section used is not capable to identify the previous invariant manifolds by simply taking initial conditions over it. Let us remark that the Poincaré surface of section selected is the one which is more likely to be crossed, as it is defined along the minimum energy path, i.e., reaction path, of the molecular system. In the case under study, the composite Poincaré surface of section is only able to conclude that the motion is chaotic, but no further insights on the chaotic phase space structure can be inferred from it.

Still, the manifolds can be represented on the Poincaré surface of section by numerically propagating initial conditions that lie in their tangent spaces. The corresponding plot reproduces the results obtained for the Lagrangian descriptors. We have studied in detail this representation, which is certainly involved. Though the manifolds of the molecule under study are continuous structures, they show up in the Poincaré surface of section as considered in this study as different sets of disconnected lines. As expected, some of these lines disappear at the frontier of the Poincaré surface of section, which is given by the limit of accessible energy, and emerge on another part of the boundary. However, in some cases, the manifolds disappear along the edge of the Poincaré surface of section, and then emerge as closed lines inside it. This intriguing and complex behavior is a consequence of the high nonlinearities in the potential energy surface, which has a strong influence on the dynamics, something that becomes clearly manifests when one uses a three dimensional plot of the manifolds. This kind of higher dimensional representation may also explain the involved shape that the invariant manifolds have when represented on the Poincaré surface of section of other molecular systems, such as LiCN, HCN or HO₂.

CRedit authorship contribution statement

F. Revuelta: Software, Investigation, Writing – original draft, Writing – review & editing. **F.J. Arranz:** Software, Investigation, Writing – original draft, Writing – review & editing. **R.M. Benito:** Conceptualization, Writing – review & editing. **F. Borondo:** Conceptualization, Writing – review & editing.

Declaration of competing interest

The authors declare that they have no known competing financial interests or personal relationships that could have appeared to influence the work reported in this paper.

Data availability

Data will be made available on request.

Acknowledgments

This work has been partially supported by the Grants PID2021-122711NB-C21 and CEX2019-000904-S funded by MCIN/AEI/10.13039/501100011033, by the People Programme (Marie Curie Actions) of the European Union's Horizon 2020 Research and Innovation Program under Grant No. 734557, and by the Comunidad de Madrid, Spain under the Grant APOYO-JOVENES-4L2UB6-53-29443N (GeoCoSiM) financed within the Plurianual Agreement with the Universidad Politécnica de Madrid, Spain in the line to improve the research of young doctors. The authors also acknowledge computing resources at the Magerit Supercomputer of the Universidad Politécnica de Madrid.

References

- [1] Lee J, Crampton KT, Tallarida N, Apkarian VA. *Nature* 2019;568:78–82.
- [2] Sullivan JP, Gilbert SJ, Surko CM. *Phys Rev Lett* 2001;86:1494–7.
- [3] Crim FF. *Proc Natl Acad Sci* 2008;105(35):12654–61.
- [4] Hare SR, Bratholm LA, Glowacki DR, Carpenter BK. *Chem Sci* 2019;10:9954–68.
- [5] Schwartz SD. Theoretical methods in condensed phase chemistry. *Progress in theoretical chemistry and physics*, 1st ed.. Springer; 2002..
- [6] Lichtenberg AJ, Lieberman MA. Regular and stochastic motion. *Applied mathematical sciences*, vol. 38, Springer; 2010..
- [7] Celletti A. Stability and chaos in celestial mechanics. *Springer praxis books*, 1st ed. Springer-Verlag Berlin Heidelberg; 2010..
- [8] Froeschlé C, Gonczi R, Lega E. *Planet Space Sci* 1997;45:881–6.
- [9] Froeschlé C, Lega E. *Celestial Mech Dynam Astronom* 2000;78(1):167–95.
- [10] Skokos C. *J Phys A* 2001;34(47):10029–43.
- [11] Benitez P, Losada JC, Benito RM, Borondo F. *Phys Rev E* 2015;92:042918.
- [12] Cincotta PM, Simó C. *Astron Astrophys Suppl Ser* 2000;147(2):205–28.
- [13] Cincotta P, Giordano C, Simó C. *Physica D* 2003;182(3):151–78.
- [14] Jiménez-Madrid JA, Mancho AM. *Chaos* 2009;19(1):013111.
- [15] Mendoza C, Mancho AM. *Phys Rev Lett* 2010;105:038501.
- [16] Craven GT, Hernandez R. *Phys Chem Chem Phys* 2016;18:4008–18.
- [17] Patra S, Keshavamurthy S. *Phys Chem Chem Phys* 2018;20:4970–81.
- [18] Revuelta F, Benito RM, Borondo F. *Phys Rev E* 2019;99:032221.
- [19] Revuelta F, Benito RM, Borondo F. *Phys Rev E* 2021;104:044210.
- [20] Uzer T, Jaffé C, Palacián J, Yanguas P, Wiggins S. *Nonlinearity* 2002;15(4):957–92.
- [21] Bartsch T, Hernandez R, Uzer T. *Phys Rev Lett* 2005;95:058301.
- [22] Bartsch T, Moix JM, Hernandez R, Kawai S, Uzer T. *Adv. Chem. Phys. John Wiley & Sons, Ltd; 2008, p. 191–238.*
- [23] Revuelta F, Bartsch T, Garcia-Muller PL, Hernandez R, Benito RM, Borondo F. *Phys Rev E* 2016;93:062304.
- [24] Junginger A, Garcia-Muller PL, Borondo F, Benito RM, Hernandez R. *J Chem Phys* 2016;144(2):024104.
- [25] Párraga H, Arranz FJ, Benito RM, Borondo F. *J Phys Chem A* 2018;122:3433–41.
- [26] Mancho AM, Wiggins S, Curbelo J, Mendoza C. *Commun Nonlinear Sci Numer Simul* 2013;18(12):3530–57.
- [27] Arranz FJ, Seidel L, Giralda CG, Benito RM, Borondo F. *Phys Rev E* 2010;82:026201.
- [28] Párraga H, Arranz FJ, Benito RM, Borondo F. *J Chem Phys* 2013;139(19):194304.
- [29] Waalkens H, Burbanks A, Wiggins S. *J Chem Phys* 2004;121:6207–25.
- [30] García-Sánchez G, Mancho AM, Wiggins S. *Commun Nonlinear Sci Numer Simul* 2022;104:106016.
- [31] Lopesino C, Balibrea-Iniesta F, Wiggins S, Mancho AM. *Commun Nonlinear Sci Numer Simul* 2015;27(1):40–51.
- [32] Cvitanović P, Artuso R, Mainieri R, Tanner G, Vattay G. *Chaos: Classical and quantum*. Copenhagen: Niels Bohr Inst.; 2016.
- [33] Eckhardt B, Wintgen D. Indices in classical mechanics. *J Phys A: Math Gen* 1991;24(18):4335–48.
- [34] Revuelta F, Vergini E, Benito RM, Borondo F. *J Phys Chem A* 2016;120(27):4928–38.
- [35] Bartsch T, Revuelta F, Benito RM, Borondo F. *Phys Rev E* 2019;99:052211.
- [36] Feldmaier M, Junginger A, Main J, Wunner G, Hernandez R. *Chem Phys Lett* 2017;687:194–9.
- [37] García-Garrido VJ, Naik S, Wiggins S. *Int J Bifur Chaos* 2020;30(04):2030008.